# Theory of nonequilibrium quantum transport and energy dissipation in terahertz quantum cascade lasers

T. Kubis,* C. Yeh, and P. Vogl
*Walter Schottky Institute, Technische Universität München, Am Coulombwall 3, 85748 Garching, Germany*

A. Benz, G. Fasching, and C. Deutsch
*Photonics Institute and Center for Micro- and Nanostructures, Vienna University of Technology, Gusshausstrasse 29/387, A-1040 Vienna, Austria*

(Received 23 April 2009; published 22 May 2009)

We analyze theoretically several crucial performance aspects of terahertz quantum cascade lasers, such as the impact of doping on the threshold current, the relative importance of the various scattering mechanisms, and the balance of coherent transport and realistic energy dissipation. We have developed a fully self-consistent model for stationary charge transport based on nonequilibrium Green's function theory that takes into account incoherent scattering with phonons, impurities, and rough interfaces as well as electron-electron scattering in the Hartree approximation, but does not *a priori* assume the electron distributions to follow the periodicity of the quantum cascade laser (QCL) structure. The theoretical results show excellent quantitative agreement with experimental data. We find scattering at rough interfaces to strongly affect electronic transport and efficiently limit the optical gain. Our results also indicate that a large portion of the current is maintained by coherent multibarrier tunneling. We show that this dominant coherent transport may lead to electron distributions that do not follow the periodicity of the QCL.

DOI: 10.1103/PhysRevB.79.195323 PACS number(s): 73.23.−b, 72.20.−i, 78.67.Pt

## I. INTRODUCTION

The terahertz (THz) spectral region offers a wide range of scientific and commercial applications that require high power and coherent sources within a narrow band.[1] THz quantum cascade lasers (QCLs) have proven to be the most promising source to fulfill these requirements. Since the first presentation of a THz-QCL by Köhler *et al.*,[2] significant progress has been achieved in optimizing the THz-QCL design.[3–6] However, we still lack a thorough understanding of the fundamental physical processes in THz-QCLs that is essential to extend the operating conditions and to improve the performance of THz-QCLs. Theoretical studies of transport in midinfrared QCLs have shown that coherent effects play a minor role compared to rapid electron dephasing.[7] Even in the THz regime, semiclassical solutions of the Boltzmann equation have proven to describe the transport in QCLs reasonably well.[8] However, coherent tunneling is expected to become more important when the laser emission frequency is reduced to a few meV. In order to investigate these effects in QCLs, several quantum transport models based on density matrix approaches and nonequilibrium Green's functions have been developed.[9–11] All of these approaches share a common *a priori* assumption, namely, the strict periodicity of the electronic states and their occupancy. To be precise, the electronic resonance states are assumed to be offset by an amount equal to $eFa$ in each QCL period, where $F$ is the electric field and $a$ is the QCL period, but equally occupied in each period. While the use of such periodic boundary conditions greatly simplifies the analysis, it limits the solutions to a small subset of the Hilbert space. Nonperiodic effects, such as coherent tunneling through extended states across one or several QCL periods, hot electron effects, or differences near source and drain contacts are left out by such an approach. The transport equations are solved in a field- and/or device-dependent basis and take only into account electronic states that are well confined within a single or a few QCL periods.[9] As a consequence, it is not possible to turn off selectively inelastic scattering channels, or consider open quantum devices with leads.

In this paper, we present a self-consistent nonequilibrium Green's function method (NEGF) for stationary charge transport in *open* quantum systems that are connected to dissipative leads. Our method differs from previous[10,12–14] NEGF implementations for QCLs in several ways. First, we use a real space basis that is not field dependent and provides a uniform and device-independent resolution of the Green's functions in space and energy. This guarantees current conservation regardless of the implemented complexity of the scattering self-energies[15] and allows us to consider limiting cases including spatially homogeneous systems. Second, we do not impose field-periodic boundary conditions. Instead, the electrons enter and leave the device via traveling eigenstates of the semi-infinite leads. This allows us to capture nonperiodic phenomena as well as investigate spatially extended, energetically higher lying states. In the leads, the electrons are assumed to remain in equilibrium which unambiguously defines the applied bias, regardless of the dissipation within the device.[16] This allows us to selectively turn on and off some or all scattering mechanisms and analyze their relative importance. Third, we implement the scattering mechanisms in their full momentum and energy dependence and do not rely on the commonly used approximation of momentum independent scattering matrix elements.[9] The only significant simplification that we are forced to use is related to the fact that we can explicitly calculate only a few active QCL periods. To this end, we have developed a model for the contacts that mimics the effect of many QCL periods

 

by modifying the density of states within the lead regions. We find excellent agreement of the calculated current versus voltage (*I-V*) characteristics with published experimental data up to and closely above threshold.[17] Our model also successfully predicts the emission frequency and the observed trends in the threshold current as a function of doping both in the linear and superlinear regime quantitatively. We also find a significant effect of the interface roughness on the optical gain and the current density.

In Sec. II, we briefly introduce the governing equations and specify the scattering self-energies and the boundary conditions for the electrostatic potential and the Green's functions, respectively. In addition, the calculation of optical gain and the numerical details are presented. In Sec. III, we compare the calculated results with available experimental data. We interpret our numerical results in detail in Sec. IV. Here, we analyze the individual influence of the various scattering mechanisms. Finally, we summarize our findings in Sec. V.

## II. METHOD

### A. Fundamentals

We use the nonequilibrium Green's function method to calculate stationary electronic transport and optical gain up to the threshold current in THz-QCLs.[18–20] All QCLs are considered as laterally homogeneous quantum well heterostructures. The electronic structure is represented in terms of a single-band effective mass model with an effective mass that depends on the growth coordinate $z$ and the energy $E$ in order to be able to incorporate nonparabolicity effects. Thus, the single-band conduction-electron Hamiltonian is given by

$$H_0 = \frac{-\hbar^2}{2}\frac{\mathrm{d}}{\mathrm{d}z}\frac{1}{m^*(z,E)}\frac{\mathrm{d}}{\mathrm{d}z} + \frac{\hbar^2 k_\parallel^2}{2m^*(z,E)} + E_c(z) - e\Phi(z), \tag{1}$$

where $k_\parallel$ is the lateral electron momentum, $\Phi(z)$ the electrostatic potential, and $E_c(z)$ denotes the material and position dependent conduction band offset. Within the NEGF formalism, we represent a QCL as an open quantum mechanical system that is characterized by four coupled partial differential equations for the electronic retarded and lesser Green's functions $G^R, G^<$, respectively. In operator form, they read

$$G^R = (E - H_0 - \Sigma^R)^{-1},$$

$$G^< = G^R \Sigma^< G^{R\dagger},$$

$$\Sigma^< = G^< D^<,$$

$$\Sigma^R = G^R D^R + G^R D^< + G^< D^R. \tag{2}$$

Here, $D$ is the sum of all environmental Green's functions that incorporate phonons, impurities, and interface roughness, and $\Sigma$ denote the self-energies. The solutions of Eq. (2) in real space do not require one to solve any kind of eigenvalue problem. Therefore, an energy-dependent mass in the Hamiltonian $H_0$ does not increase the complexity of the solution. However, for the occupied laser states relevant for this paper, the band structure can be treated as parabolic.[21] All the Green's functions $G(z,z',k_\parallel,E)$ and self-energies $\Sigma(z,z',k_\parallel,E)$ are taken as functions of two spatial coordinates $z,z'$, the lateral momentum $k_\parallel$, and the energy $E$. Once the Green's functions are known, the observables such as the spatially resolved density $n(z)$ and current density $j(z)$ can be determined straightforwardly,

$$n(z) = \int \mathrm{d}E n(z,E) = \frac{2}{(2\pi)^3}\mathrm{Im}\int \mathrm{d}E \int \mathrm{d}\vec{k}_\parallel G^<(z,z,k_\parallel,E), \tag{3}$$

$$\begin{aligned} j(z) &= \int \mathrm{d}E j(z,E) \\ &= -\lim_{z'\to z}\int \mathrm{d}E \int \mathrm{d}\vec{k}_\parallel \frac{\hbar e}{(2\pi)^3 m^*(z,E)} \\ &\quad \times \mathrm{Re}\left(\frac{\mathrm{d}}{\mathrm{d}z} - \frac{\mathrm{d}}{\mathrm{d}z'}\right) G^<(z,z',k_\parallel,E). \end{aligned} \tag{4}$$

For later reference, these equations define the spatially and energy resolved density $n(z,E)$ and current density $j(z,E)$, respectively.

### B. Scattering self-energies

We include scattering of the carriers by polar optical phonons, acoustic phonons, charged impurities, and rough interfaces in terms of retarded and lesser self-energies $\Sigma^R, \Sigma^<$ in Eq. (2). We use the bulk phonon approximation which has been shown to be well justified for QCLs (Ref. 22) and assume the phonons to remain at the lattice temperature of 40 K (see Sec. III C). The material parameters are taken from Ref. 23. The strongly inelastic polar optical phonon scattering has been implemented by including its full three-dimensional momentum and energy dependence according to Ref. 19 and screened by the Debye screening length.

The acoustic phonon scattering is usually approximated as elastic scattering mechanism. Our implementation goes one step further by using the following procedure. In the high-temperature approximation for the acoustic phonon occupation factors and by using $\omega_q = v_s q$ ($\omega_q$ is the acoustic phonon frequency and $v_s$ the sound velocity), the longitudinal acoustic phonon self-energies $\Sigma^<_{\mathrm{ac}}$ can be written as

$$\begin{aligned} \Sigma^<_{\mathrm{ac}}(z,z',k_\parallel,E) &= \frac{1}{(2\pi)^3}\frac{k_B T D^2}{2\rho v_s^2}\int \mathrm{d}\vec{q}_\parallel \mathrm{d}q_z e^{iq_z|z-z'|} \\ &\quad \times [G^<(z,z',|\vec{k}_\parallel - \vec{q}_\parallel|, E+\hbar\omega_q) \\ &\quad + G^<(z,z',|\vec{k}_\parallel - \vec{q}_\parallel|, E-\hbar\omega_q)]. \end{aligned} \tag{5}$$

The acoustic deformation potential and the material density are denoted by $D$ and $\rho$, respectively. Instead of omitting the energy shifts $\pm\hbar\omega_q$ in this expression, as is commonly done,[19] we replace the Green's functions by an energy-averaged form $\tilde{G}^<$ and $\tilde{G}^R$

$$\tilde{G}(z,z',q_\parallel,E) = \frac{1}{2\hbar\omega_D}\int_{E-\hbar\omega_D}^{E+\hbar\omega_D} dE' G(z,z',q_\parallel,E'), \quad (6)$$

with the Debye frequency $\omega_D$. In this way, the acoustic phonon scattering can dissipate energy.

The standard expression for the impurity scattering self-energy $\Sigma_{\text{imp}}$ (for $\Sigma^R$ and $\Sigma^<$, respectively) reads[19]

$$\Sigma_{\text{imp}}(z,z',k_\parallel,E) = \frac{e^4}{16\pi^2\varepsilon_0^2\varepsilon_r^2}\int d\vec{q}_\parallel F(z,z',|\vec{k}_\parallel - \vec{q}_\parallel|) \times G(z,z',q_\parallel,E), \quad (7)$$

$$F(z,z',p_\parallel) = \int dz'' N_D(z'') \frac{e^{-\sqrt{q_D^2+p_\parallel^2}(|z-z''|+|z'-z''|)}}{q_D^2+p_\parallel^2}, \quad (8)$$

where $N_D(z)$ is the ionized impurity concentration, and both the inverse Debye screening length $q_D$ and the static dielectric constant $\varepsilon_r$ represent device averaged values. We have checked that the following approximation mimics the full $z,z'$ dependence of the self-energy and grossly reduces the numerical evaluation for the integrals. We replace the integral $F$ in this expression Eq. (8) by

$$F(z,z',p_\parallel) \approx N_D(z,z')\int dz'' \frac{e^{-\sqrt{q_D^2+p_\parallel^2}(|z-z''|+|z'-z''|)}}{q_D^2+p_\parallel^2},$$

$$N_D(z,z') = \begin{cases} N_D(z), & \text{for } z = z' \\ \dfrac{1}{z'-z}\displaystyle\int_z^{z'} d\zeta N_D(\zeta), & \text{elsewhere,} \end{cases} \quad (9)$$

and perform the $z''$-integral analytically. This procedure slightly overestimates charged impurity scattering whenever $z$ or $z'$ lie within the doped regions and slightly underestimate it otherwise.

The interface roughness self-energies $\Sigma_{\text{IR}}$ (again for $\Sigma^R$ and $\Sigma^<$) read for a Gaussian shaped in-plane correlation function[19]

$$\Sigma_{\text{IR}}(z,z',k_\parallel,E) = \frac{\lambda^2\delta V^2}{16\pi}\Xi(z)\Xi(z')e^{-k_\parallel^2\lambda^2/4}\int d\vec{q}_\parallel [e^{-q_\parallel^2\lambda^2/4} \times I_0(k_\parallel q_\parallel \lambda^2/2) G(z,z',q_\parallel,E)], \quad (10)$$

where $\lambda$ denotes the in-plane autocorrelation length of the roughness potential, $\delta V$ is the conduction band difference between the two adjacent materials, $I_0$ represents the modified Bessel function, and $\Xi(z)$ equals unity in a region $\delta z$ around the interface position, and vanishes otherwise. Thus, $\delta z$ is the roughness step height in the growth direction. We have also implemented an exponentially shaped in-plane correlation function, but found no significant changes (see Sec. IV A).

We now turn to the electron-electron scattering. We have included its Hartree part exactly by solving the Poisson equation together with Eq. (2) self-consistently. It has been suggested by Monte Carlo simulations that the higher-order electron-electron scattering significantly influences the transport characteristics of THz-QCLs.[24–26] In order to estimate the influence of this scattering mechanism, we have calculated the electron-electron self-energy in the static $GW_0$-approximation.[27–30] In calculating the interaction $W_0$, we assume a homogeneous electron gas with average density $n_e$ and a Boltzmann distribution function at lattice temperature $T$. We approximate the finite temperature dielectric function by its static, long wavelength limit and use average values $m^*$ and $\varepsilon_r$ for the effective mass and static dielectric constant, respectively. This yields the retarded and lesser interaction potential,

$$W_0^R(z-z',q_\parallel) = \frac{e^2}{2\pi\varepsilon_0\varepsilon_r}\int dq_z \frac{e^{iq_z(z-z')}}{q^2\varepsilon(q,0)}, \quad (11)$$

$$\varepsilon(q,0) = 1 + q^{-2}q_D^2, \quad (12)$$

$$W_0^<(z-z',q_\parallel) = -\frac{i}{2\pi^2}\frac{e^4 m^{*2} k_B T}{\varepsilon_0^2\varepsilon_r^2\hbar^4} \times \left[n_e\left(\frac{2\pi\hbar^2}{m^* k_B T}\right)^{3/2} - \frac{n_e^2}{4}\left(\frac{2\pi\hbar^2}{m^* k_B T}\right)^3\right] \times \int_{-\infty}^{\infty} dq_z \frac{e^{iq_z(z-z')}}{q(q^2+q_D^2)^2}. \quad (13)$$

In addition, we limit the energy transfer by introducing a temperature-dependent frequency cutoff. This leads to the electron-electron self-energies,

$$\Sigma_{\text{ee}}^R(z,z',k_\parallel,E) = \frac{i}{(2\pi)^3}\int dE' \int d\vec{q}_\parallel e^{-|E-E'|/k_B T} \times (G^R W_0^R + G^< W_0^R + G^R W_0^<), \quad (14)$$

$$\Sigma_{\text{ee}}^<(z,z',k_\parallel,E) = \frac{i}{(2\pi)^3}\int dE' \int d\vec{q}_\parallel e^{-|E-E'|/k_B T} G^< W_0^<, \quad (15)$$

where $G$ and $W_0$ in these expressions stand for the functions $G=G(z,z',|\vec{k}_\parallel-\vec{q}_\parallel|,E')$ and $W_0=W_0(z-z',q_\parallel)$ for both retarded and lesser functions, respectively. We restrict $|z-z'|$ in these self-energies to a typical width of a quantum well (8 nm in the present cases) since the self-energy decays rapidly beyond barriers. We note that the retarded interaction potential $W_0^R$ is much smaller than $W_0^<$. This self-energy is only a first step toward a consistent treatment of higher-order electron-electron effects because the reabsorption of dissipated energy and momentum is largely ignored so that the thermalization of propagating electrons gets overestimated in this procedure.

The self-energies contain the Green's functions that need to be determined self-consistently with Eq. (2). Unfortunately, the NEGF formalism does not automatically guarantee current conservation. As soon as one wishes to solve the Green's functions to infinite order in the self-energies by solving the Dyson equation [see Eq. (2)], the calculation of the self-energies in lowest-order Born approximation would lead to a violation of current conservation. In order to guarantee current conservation, we employ the self-consistent Born approximation that includes the scattering self-energies

to infinite order in the Green's functions and has been shown to conserve the electric current.[31] This procedure ensures that the scattering states ($G^R$), the transition probabilities between them ($\Sigma$) and their occupations ($G^<$) are calculated self-consistently with one another.

### C. Boundary conditions for QCLs

#### *1. Electrostatic boundary conditions*

We determine the electrostatic potential $\Phi(z)$ self-consistently with the electron density $n[z,\Phi]$ under the condition of global charge neutrality. This implies a solution of the Poisson equation with an equal slope of the electrostatic potential $\Phi$ at the left and the right boundary. We adjust this slope in such a way that the potential drop across the device equals the bias voltage that is defined by the difference between the chemical potentials in the leads. This results in a well-defined potential at the device boundaries. Since THz-QCLs are often only slightly doped, one obtains an almost constant slope of $\Phi$ in many cases. However, we will also consider situations with higher doping concentrations in this paper (see Sec. III B).

#### *2. Boundary conditions for the Green's functions*

We consider the QCL as an open quantum device with electrons propagating between the two reservoirs. We assume an efficient energy relaxation within the leads, so that the electrons have a Fermi distribution $f(E,\mu)$ therein. For reasons discussed in detail in Sec. III C, we use a constant lattice temperature of 40 K in the leads and in the device. We do not calculate the scattering self-energies in Eq. (2) within the leads but use a constant retarded self-energy $\Sigma^R(z,z',k_\parallel,E)=-i\hbar\delta(z-z')/2\tau_{sc}$ and the equilibrium value for the lesser self-energy $\Sigma^<=i\hbar f\delta(z-z')/\tau_{sc}$ therein. The nonlocal part of the device self-energies that leaks into the leads is cut off accordingly. We introduce a transition zone of 6 nm between the device and the leads. In this area, the Poisson equation, the Green's functions and self-energies are solved self-consistently in order to smoothen the electronic transitions between the device and the leads. The results in QCLs do not depend on the details of the self-energies within the leads due to the efficient limitation of the QCL transport by the barriers. A typical value for $\tau_{sc}$ is of the order of 0.1 ps. We would like to emphasize that scattering within the leads does play an important role in devices with low barriers close to the leads.

The computational effort for explicitly calculating the quantum transport across hundreds of QCL periods is prohibitive. Therefore, we have devised two schemes that mimic the transport through extended QCL structures reasonably accurately while limiting the calculations to one or two active periods and remaining in the framework of open systems.[19,31,32] First, we connect the device to homogeneously doped semi-infinite GaAs leads with a doping concentration within the leads that match the doping level of the widest quantum well within the QCL. In this way, artificial reflections at the boundaries are avoided. In this model that we term single periodic lead model [see Fig. 1(a)], electrons

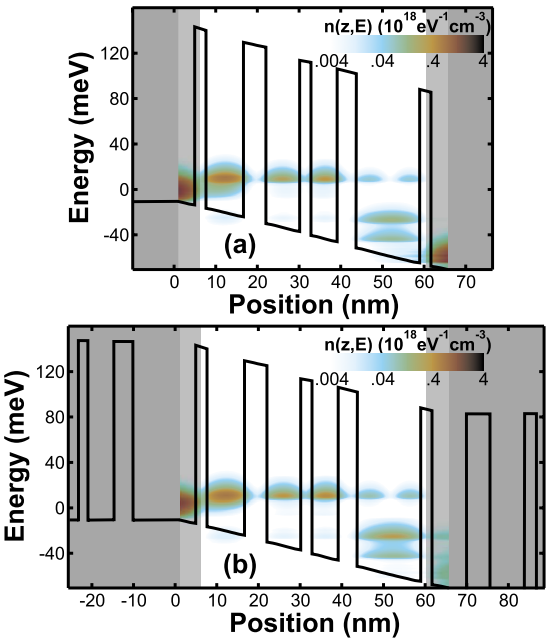


FIG. 1. (Color online) Contour plots of the energy and spatially resolved density $n(z,E)$ of the QCL structure studied in this paper, in units of $10^{18}$ eV$^{-1}$ cm$^{-3}$. The detailed material composition and dimensions will be given in Sec. III. The sheet doping density is taken to be $1.9\times10^{10}$ cm$^{-2}$. The solid lines indicate the self-consistent potential profile, the source-drain bias voltage is 50 mV per period. The zero in energy marks the chemical potential of the source. The shaded regions indicate the lead areas, including small transition regions. (a) Single periodic lead model. (b) Multiquantum well lead model.

propagate as plane waves within the field-free leads, and develop according to the full dynamics contained in Eq. (2) within the device. In the second approach, that we term multiquantum well lead model [see Fig. 1(b)], we model the QCL periods surrounding the calculated single-period device by a field-free multiquantum well structure that continues the QCL band structure into the leads.[33] In this model, the electrons in the leads effectively propagate in eigenstates of the field-free QCLs, and enter the device with a density of states that mimics the situation in a multiperiod system more realistically. Figures 1(a) and 1(b) depict the conduction band profiles (solid lines) within the device as well as within the semi-infinite leads (gray-shaded regions) and the 6 nm wide transition zones (light gray-shaded regions). In addition, these contour plots illustrate that the calculated spatially and energy resolved carrier density [see Eq. (3)] hardly differs in these two lead models. This is shown in more detail in Fig. 2 that illustrates the density $n(z,E)$ at two device positions $z=14$ nm and $z=50$ nm. This similarity explains why we have previously noticed that both models lead to similar current densities and optical gains.[33]

### D. Optical gain and threshold current

We follow the scheme of Ref. 18 for calculating the frequency-dependent absorption coefficient $\alpha(\omega)$ in the linear response approximation and for linearly polarized light

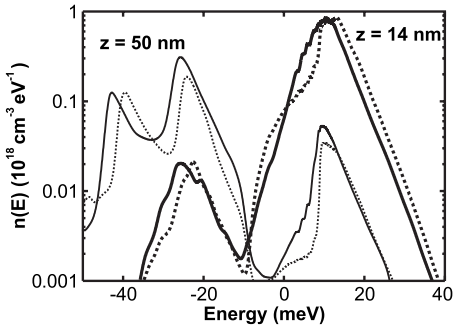


FIG. 2. Cross section of the energy resolved density of the QCL shown in Fig. 1 in the leftmost quantum well (thick lines) and rightmost quantum well (thin lines). The results obtained with the single period lead model (dotted lines) agree well with the multi-quantum well model (solid lines).

along the growth direction. This approach fully accounts for the self-consistently calculated laser states and their nonequilibrium state occupations. The optical absorption coefficient is often defined with respect to the field intensity ($\alpha_I$) rather than with respect to the field amplitude ($\alpha_A$).[34] In particular, in the gain regime one often refers to the power gain $-\alpha_I$. These quantities are related by $\alpha_I=2\alpha_A$. In this paper, all results actually show the smaller value $\alpha_A$. We have not included electron-photon vertex corrections in our model. It has been shown that vertex corrections narrow the optical linewidths and increase the peak height of the absorption coefficient in THz-QCLs but do not significantly shift the frequency where $\alpha_A(\omega)$ has its minimum.[35] Thus, our calculations do not predict quantitative values of $\alpha_A(\omega)$. The threshold current is usually defined as that current where the device averaged gain matches all external losses.[36] Since our calculations do not include external losses, we define the threshold current as that current where the device averaged gain[37] reaches transparency, i.e., $\alpha_A=0$.

### E. Numerical details

We solve equations Eq. (2) in a real space basis with a homogeneous grid spacing of $\Delta=0.9$ nm. We compensate the coarseness of this real space grid by slightly modifying the material's barrier heights in such a way that the product of their width and height is preserved. All integrals involving numerically determined Green's functions are solved with the trapezoidal quadrature method. We employ two independent self-adaptive grids for the energy $E$ and momentum $k_\parallel$ space. The initial average energy spacing matches typical resonance widths ($\sim$1 meV) and gets refined until all energy maxima in the spatial average $\int dz n(z,E)$ are resolved. However, we keep the total number of grid points fixed. Typical values that we have used for the devices in this paper are 130 energy grid points. The in-plane momentum $k_\parallel$ is first represented as an energy $E_z=E-\hbar^2k_\parallel^2/[2m^*(z=0,E)]$. These energy grid points are redistributed until all maxima of the spectral function $\mathrm{Im}[G^R(z,z,k_\parallel,E_{\max})-G^{R\dagger}(z,z,k_\parallel,E_{\max})]$ are resolved. Here, $E_{\max}$ denotes an energy that lies well above the highest occupied device state.

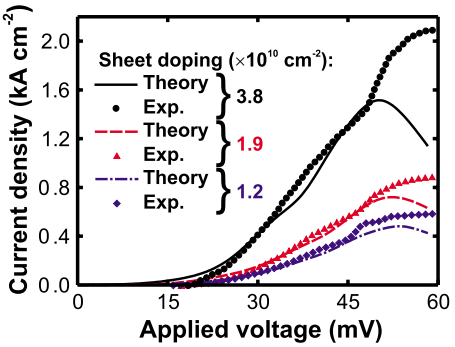


FIG. 3. (Color online) Experimental and calculated stationary current densities in units of kA $cm^{-2}$ versus applied voltage per period in mV. The sheet doping densities are $3.8\times10^{10}$ $cm^{-2}$ (dots and solid line), $1.9\times10^{10}$ $cm^{-2}$ (triangles and dashed line), and $1.2\times10^{10}$ $cm^{-2}$ (diamonds and dash-dotted line), respectively.

We initiate our iterative solution of the Green's functions with a constant electric field that corresponds to the applied bias voltage. Consequently, Eq. (2) is iterated together with the Poisson equation until the L1-norm of the relative difference in the local densities $n(z)$ of two successive undamped iterations at each device point is less than $10^{-4}$. The Poisson equation is solved with the predictor-corrector approach described in Ref. 38. This procedure guarantees well converged Green's functions and self-energies and typically results in a relative deviation of the current density $j(z)$ from its spatial device average in the range of 0.5%.

## III. RESULTS

All THz-QCLs considered in this paper consist of 271 identical periods of GaAs and $Al_{0.15}Ga_{0.85}As$ layers of the widths (30) 92 (55) 80 (27) 66 (41) 155 Å, where the values in parentheses indicate the $Al_{0.15}Ga_{0.85}As$ barriers.[17] Only the widest well is doped. The only difference between the QCL structures studied in this paper lies in the doping concentration of this well.[17] The experimental heat sink temperature is 5 K. The QCLs are designed to utilize the depletion of the lower laser level by emission of LO-phonons.[39]

### A. Relevant scattering mechanisms

Figure 3 shows a comparison of the measured[17] and calculated *I-V* characteristics of the QCL with different doping densities. As can be seen from these results, our model agrees excellently with the experimental data. This suggests that our treatment and inclusion of LO-phonon and acoustic phonon scattering, charged impurity and interface roughness scattering, and electron-electron scattering in the Hartree approximation captures the relevant physics of carrier transport in THz-QCLs. The higher-order electron-electron scattering self-energy has not been included in these calculations; for a discussion of its effect, see Sec. IV B. The calculated negative differential resistivity above the threshold bias, i.e., above 46 mV bias per period, originates from misaligned laser states. The experimental data also indicate misalignment effects, but they occur at higher current densities. The

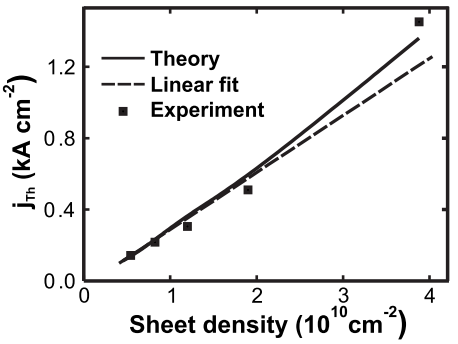


FIG. 4. Comparison of measured and calculated threshold current density $j_{Th}$ in units of kA cm$^{-2}$ as a function of sheet density in units of $10^{10}$ cm$^{-2}$. The full line indicates the present theory, the squares are experimental data of Ref. 17. A linear fit to the calculated data for low sheet densities (dashed line) illustrates the deviation from linearity at higher doping.

present theory ignores the coupling of the carriers to the laser field. This approximation may underestimate the current density above threshold. Larger bias voltages may also lead to hot electrons that are not fully captured by our lead models.

### B. Threshold current versus sheet doping density

The calculations yield a linear increase in the threshold current at low doping densities. For sheet densities above $2\times10^{10}$ cm$^{-2}$, we obtain a slightly superlinear behavior. This trend has been observed experimentally for the presently studied THz-QCLs (Ref. 17) as well as for similar structures.[40] As can be seen in Fig. 4, our NEGF calculations excellently reproduce the observed[17] trend in the threshold current as a function of the doping concentration, both for the linear as well as for the superlinear regime. The increase in the threshold current with doping has been assigned to optical losses due to free-carrier absorption[40,41] and to a reduced upper state lifetime due to electron-phonon scattering.[41] However, simple model calculations have indicated that the free-carrier absorption cannot explain the slope in the threshold for low doping.[42] Our calculations show that the doping dependence of the threshold current is solely determined by changes in the level alignments. The mechanisms that are responsible for gain in the presently studied QCL structures are illustrated in Fig. 5. It depicts a contour plot of the energy and spatially resolved spectral function $A(z,E)=i[G^R(z,z,0,E)-G^{R\dagger}(z,z,0,E)]$ of a QCL with a sheet doping density of $1.9\times10^{10}$ cm$^{-2}$ for vanishing lateral momentum $k_{\|}=0$ and a bias voltage of 50 mV per period. This voltage lies slightly above threshold. The maxima of the spectral function represent resonant states. Most noticeably, all states show a finite width and a fine structure that result from the coupling of all well states with one another. The upper laser level (labeled by 4) which is predominantly an antibonding state is aligned with the confined state 5 in the leftmost source-sided quantum well and therefore gets filled by resonant tunneling. The lower laser level 3 gets efficiently emptied by two mechanisms. First, the bonding state 3 is aligned with the states 2 and 2′ of the rightmost well which allows its coherent depletion by tunneling. Second, the energy difference between this state and the lowest resonance state (1) matches approximately the energy of an LO-phonon (36 meV) which leads to an additional depletion by the resonant emission of LO-phonons. In the regime of low doping densities, the alignment conditions are unaffected by the carrier concentration. Therefore, the threshold voltage remains constant and the current depends linearly on the carrier density in this regime as can be deduced from Fig. 4.

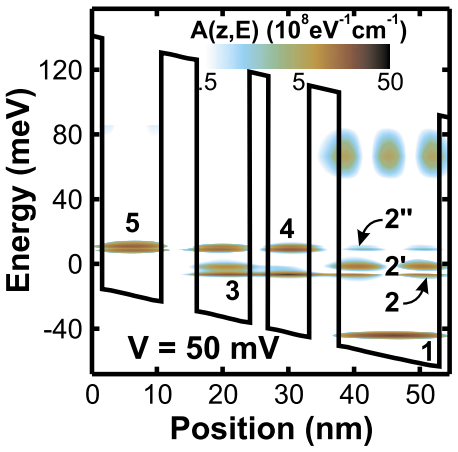


FIG. 5. (Color online) Contour plot of the spectral function $A(z,E)$ of the QCL with sheet doping density of $1.9\times10^{10}$ cm$^{-2}$, in units of $10^8$ eV$^{-1}$ cm$^{-1}$, as a function of position $z$ in nm and energy $E$ in meV. The zero in energy marks the chemical potential of the source. The applied bias voltage is 50 mV per period. The solid line indicates the self-consistent potential profile. The spectral function is only shown within the energy interval from −70 to 110 meV. The labels number the relevant resonances that are discussed in the main text.

The inhomogeneous spatial charge distribution at higher doping concentrations causes a nonlinear conduction band profile. There is a slightly positive space charge in the widest quantum well that lowers its band edge including the states 1 and 2′ by a few meV. This effect improves the alignment of states 3 and 2′ with one another, leading to a superlinear enhancement of the current with doping density. This prediction is nicely confirmed by the experimental data, as shown in Fig. 4. Similar influence of the alignment conditions on the current density has been seen before in midinfrared QCLs.[43,44] In addition, the improved alignment of the states 2′ and 3 at higher doping densities causes an enhanced anticrossing between these states and reduces the calculated peak gain energy by approximately 2 meV.

### C. Heating of the QCL during pulsed mode operation

The comparison between experiment and theory in Fig. 3 allows us to extract information about the heating of the device as a function of the bias voltage in the experiments. Propagating electrons in QCLs dissipate energy and cause the lattice temperature to deviate from the heat sink temperature of 5 K. Callebaut *et al.*[45] and Vitiello *et al.*[46] have shown that the lattice temperature increases in pulsed mode by approximately 20–50 K above the heat sink temperature of 5 K, in spite of the 100 ns pulses that have been used in the

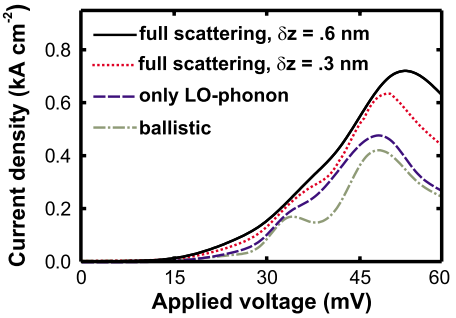


FIG. 6. (Color online) Calculated $I$-$V$ characteristics of the QCL with a sheet doping density of $1.9\times10^{10}$ cm$^{-2}$. The green dash-dotted line is a purely ballistic calculation without scattering self-energies. For the blue dashed line, polar optical phonon scattering has been included. All scattering mechanisms with a roughness step height of $\delta z=0.6$ nm lead to the black solid curve. The red dotted curve differs from the black full line only by a reduced roughness step height of $\delta z=0.3$ nm.

experiments of Ref. 42. Therefore, we have assumed a lattice temperature of 40 K throughout the device and including the leads, irrespective of the applied bias. At low bias, this assumption may slightly overestimate the device temperature. Indeed, the predicted current slightly overestimates the observed one for voltages below 25 mV per period (see Fig. 3) since higher temperatures facilitate the tunneling processes. At higher voltages, on the other hand, our model reproduces the measured current density up to threshold.

## IV. DISCUSSION

### A. Comparison of scattering mechanisms

Incoherent scattering mechanisms are known to be crucial for the transport characteristics of THz-QCLs.[8,18,24] It is therefore relevant to study the individual contributions of the various scattering mechanisms and analyze their relative importance. In Fig. 6, we show several calculated $I$-$V$ characteristics. The sheet doping concentration of the widest QCL well amounts to $1.9\times10^{10}$ cm$^{-2}$. The solid curve shows the most realistic calculation where phonon, impurity, interface roughness, and electron-electron scattering in the Hartree approximation have been fully included. This curve equals the dashed line in Fig. 3. The dash-dotted curve shows the limiting case where all scattering self-energies have been artificially turned off ("ballistic regime"). The two maxima near 35 and 50 mV correspond to states that extend across the entire QCL period for these voltages. They are highly delocalized and therefore provide efficient coherent current channels. As shown in Fig. 5 at a voltage of 50 mV, the upper laser level (4) is poorly confined and leaks into the collector well (2″). As a consequence, the electronic tunneling out of the upper laser level is only slightly suppressed but not completely blocked. In summary, we find that almost 50% of the realistic current originates in coherent multibarrier tunneling. This is a somewhat surprising result since previous studies of shorter-wavelength QCLs have suggested that the transport is predominantly incoherent.[7]

The dashed curve in Fig. 6 shows the current where all scattering mechanisms but LO-phonon scattering have been turned off. This leads to only a small increase in the current compared to the ballistic results due to three effects. First, the leakage of the upper laser level into the collector well carries most of the current. Second, the lower laser level (3 in Fig. 5) remains almost empty due to the lack of a resonant state in the injector well at this energy. Since, in addition, the lower states 2 and 2′ are also almost empty, phonon emission mostly occurs between the upper laser level 4 and the lowest collector state 1. This process is not efficient since the energy separation between these levels amounts to approximately 50 meV and thus exceeds the optical phonon energy. There is, in addition, some optical phonon emission between states 2″ and 1 within the collector well, but this only forks the current channels and does not increase the current.

The isolated effect of charged impurity and acoustic phonon scattering is not shown in Fig. 6 because they have a small influence on the current density. By contrast, we find a marked influence of the interface roughness scattering which we now discuss in some detail.

#### *Influence of rough interfaces in THz-QCLs*

Figure 6 shows two $I$-$V$ curves that are labeled by "full scattering." Both curves include the electron-electron scattering in the Hartree approximation as well as the scattering by phonons, impurities, and rough interfaces. Yet, they differ in the assumed interface roughness step height $\delta z$. The in-plane roughness correlation length is assumed to be $\lambda=8$ nm in both cases.[47–49] The value of $\delta z=0.6$ nm corresponds to a roughness of $\pm1$ monolayer in the growth direction and lies within typical experimental data.[47–50] We find a continuous increase in the current with interface roughness; the zero roughness case is shown by the dashed curve, and an intermediate value of $\delta z=0.3$ nm is depicted as well.

Scattering by rough interfaces is an elastic scattering mechanism that randomizes the electron in-plane momentum $k_{\|}$ by an amount of $\lambda^{-1}$. This corresponds to an energy randomization of approximately 9 meV. Consequently, this scattering mechanism enables transitions of electrons from the upper laser level (4) to the collector states (2, 2′) as can be deduced from Fig. 5. This effect significantly enhances the leakage current of electrons because the density of states of the states 2 and 2′ are much larger than of 2″. In addition, this effect reduces the occupation inversion and the optical gain significantly since the states 2 and 2′ are aligned with the lower laser state 3 close to threshold. This effect is shown in Fig. 7 that displays the calculated cross sections of the absorption coefficient $\alpha_A$ as a function of the photon energy $E_{\text{photon}}$ in the center of the QCL in Fig. 5 ($z=28$ nm) and for various roughness step heights $\delta z$. The calculated gain maxima match the measured emission energy of 13 meV very well. The gain is maximal for smooth interfaces and gets reduced by almost an order of magnitude by realistic interface roughness scattering. Thus, rough interfaces effectively suppress the formation of a laser which is in accord with experimental observations.[50]

Our results seem at variance with previous NEGF findings of Nelander and Wacker[51] for similar QCL structures. These

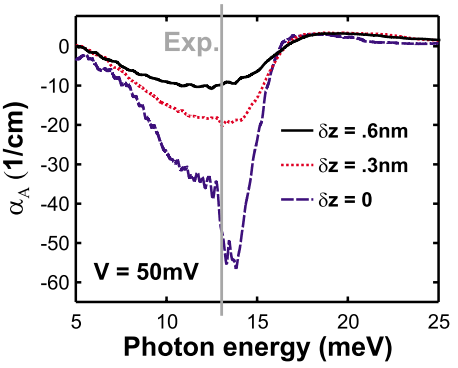


FIG. 7. (Color online) Calculated absorption coefficient $\alpha_A(z, E_{\text{Photon}})$ in the center of the QCL period at a bias of 50 mV for various roughness step heights in nm: $\delta z$=0.6 nm (black solid), $\delta z$=0.3 nm (red dotted), and $\delta z$=0, i.e., smooth interfaces (blue dashed). The gray line marks the experimental photon emission energy.

authors do not see a significant influence of rough interfaces on the current for a correlation length of $\lambda$=10 nm and a step height $\delta z$=0.24 nm. While their roughness model slightly differs from ours (exponential instead of Gaussian correlation), we have checked that this difference is insignificant and does not influence our results. In addition, these authors obtain a large effect due to charged impurity scattering. The discrepancies may be caused by the assumption of momentum independent scattering potentials in Ref. 51.

### B. How periodic is a QCL?

In a finite electric field, a periodic carrier distribution can only build up in a cascade structure if there is a sufficient amount of inelastic scattering that resets the carrier distribution in each injector well to the same set of values. For a doping density of $1.9\times10^{10}$ cm$^{-2}$, we find a threshold voltage of 46 mV/period. Thus, the electrons have to dissipate 46 meV in each QCL period in order to maintain a periodic distribution. However, the emission of a single LO-phonon within one period dissipates only an energy of 36 meV. Consequently, the remaining 10 meV have to be dissipated by other processes. Possible candidates are higher-order electron-electron (e-e) scattering or/and the emission of acoustic phonons. The emission rate of photons up to threshold is known to be very inefficient ($\sim$0.1 $\mu$s$^{-1}$). We have seen above that scattering with acoustic phonons plays only a secondary role. Thus, the only plausible candidate appears to be the e-e scattering. As will be discussed below, however, even this scattering mechanism seems not capable of dissipating this amount of energy.

In order to investigate this problem in more detail, we have performed elaborate calculations that take into account two full QCL periods explicitly as active open device, attached to multiquantum well leads as discussed in Sec. II C. In this way, we do not assume an electronic carrier distribution that follows the QCL period *a priori*. We assume a sheet doping density of $1.9\times10^{10}$ cm$^{-2}$ and focus on the situation for an applied bias voltage of 52 mV per QCL period, i.e., just slightly above the threshold voltage. Our key finding is

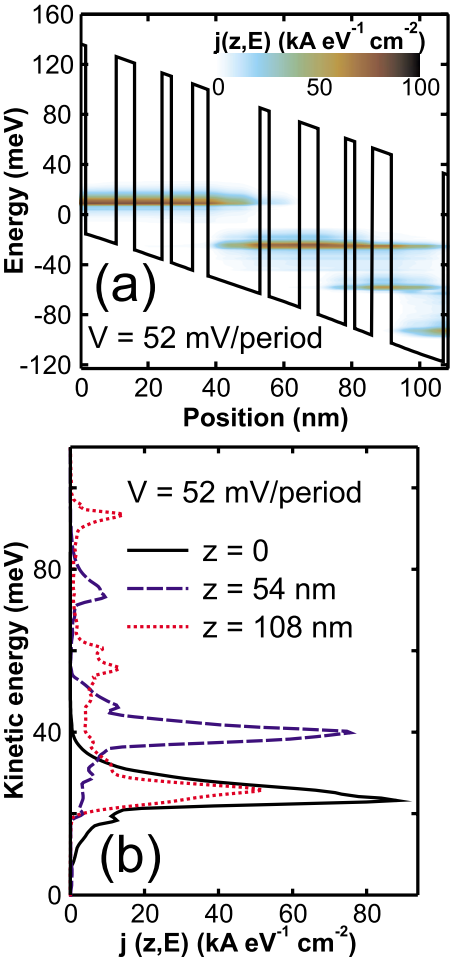


FIG. 8. (Color online) (a) Conduction band profile (solid line) and contour plot of the energy and spatially resolved current density $j(z,E)$ of the QCL with a sheet doping density of $1.9\times10^{10}$ cm$^{-2}$ at a voltage of 52 mV per period. The zero in energy marks the chemical potential of the source. Here, two QCL periods are explicitly taken into account. (b) Cross section of the energy and spatially resolved current density in the leftmost (black solid) barrier, the central barrier (blue dashed), and the rightmost (red dotted) device barrier, respectively.

that carrier distributions build up that are commensurable with the geometric QCL period but with a *commensurability period that is larger than a single QCL period* and extends over two or even more QCL periods. This result implies that the number of emitted LO phonons is no longer strictly one per geometric QCL period as we are now going to show. Figure 8(a) shows a contour plot of the energy and spatially resolved current density $j(z,E)$ as defined in Eq. (4). To better guide the eyes, the conduction band profile of the device (solid line) is depicted as well. The spatially resolved current density is a quantity that vividly illustrates coherent transport as well as energy dissipation processes. If there is no energy dissipation, the contour plot of $j(z,E)$ would only show one or several horizontal (i.e., spatially constant) stripes that extend across the entire device. Any disruptions of these stripes, on the other hand, mark positions where LO phonon emissions set in. A sequence of three emitted LO-phonons can easily be identified in the figure. This result implies the

resonant emission of three LO-phonons across two QCL periods and a net energy dissipation of $3\times36=108$ meV in the device which differs from the voltage drop of $2\times52=104$ meV only by 4 meV which lies in the range of acoustic phonon energies. To illustrate this result in more detail, Fig. 8(b) depicts cross sections of the spatially resolved current density at three prominent device positions: initial injection region ($z=0$), end of first QCL period ($z=54$ nm), and final collector region ($z=108$ nm). Since the total current density is a conserved quantity, the area under each of the three curves is the same. For each curve, the energy is counted relative to the local conduction band edge. If the electronic carrier distribution was perfectly periodic in each QCL period, the three curves in Fig. 8(b) would lie on top of each other. By contrast, the calculations show that the electrons have emitted only one LO-phonon (36 meV) at the end of the first period. Instead of dissipating the remaining 16 meV, the electrons enter the second period with a higher energy which leads to the shift of the peak in $j(z,E)$ at $z=54$ nm. Near the end of the second QCL period, the electrons have accumulated enough energy to actually emit two LO-phonons. This resets the main portion of the carrier distribution almost completely to its original value, as shown by the dotted line in Fig. 8(b). Since all electronic states have a finite width, the remaining small energy difference can be compensated by LA scattering. The smaller peaks in $j(z,E)$ at $z=108$ nm reflect the ballistic portion of transport and lie exactly one and two LO phonon energies above the main peak. In summary, we find that the carrier distribution in a THz-QCL does not simply follow the geometric periodicity of the structure but develops commensurable and conceivably even incommensurable distributions as a function of bias. The results of the calculation shown in Fig. 8 do not include higher-order e-e interactions. It is known in literature that the inelastic electron-electron interaction can thermalize the intrasubband electron distribution.[26,52] In order to estimate whether the inelastic e-e scattering can relax the electrons and restore the periodicity of the carrier distribution to a single QCL period, we have calculated the Green's functions including the approximated self-energies of Eqs. (14) and (15). The scattering rates that result from this self-energy are comparable with those of the resonant emission of LO-phonons, in agreement with similar findings of Monte Carlo simulations.[25] Nevertheless, we find the e-e interaction to be unable to thermalize the nonequilibrium subband distribution sufficiently strongly. In particular, we find the main peak of the energy resolved current density in the center of the device in Fig. 8(b) to be shifted downward by only approximately $k_BT=3.4$ meV to lower kinetic energies and a broadening of this peak by approximately twice this amount.

We would like to emphasize that the total current is insensitive to these commensurability effects and therefore not a suitable observable for detecting them for the weak doping levels that are characteristic of THz-QCLs. This explains the good agreement we have obtained with a single-period model as shown in Fig. 3. The peaks in the integral current density only reflect the energetic position and widths of the resonant states. Since the doping levels are quite low, these positions are insensitive to small changes in the local carrier occupancies.

## V. CONCLUSION

We have developed a fully self-consistent nonequilibrium Green's function theory for the stationary electron transport in THz-QCLs. We consider the QCLs as open quantum devices, which allow us to analyze the relative importance of the various scattering mechanisms in great detail and perform calculations that do not *a priori* assume the electron distribution to exhibit the same periodicity as the QCL structure. Our model calculations excellently reproduce the experimental *I-V* characteristics and the peak gain energy for a typical GaAs/AlGaAs THz-QCL. We are able to elucidate and explain crucial properties of THz-QCLs such as the doping dependence of the threshold current, the relative importance of various incoherent transport mechanisms, and the formation of optical gain. We find that about 50% of the current is caused by coherent multibarrier tunneling. In addition, we find interface roughness to significantly increase the stationary current density and to simultaneously grossly reduce the optical gain. Charged impurity, acoustic phonon, as well as higher-order e-e interactions are found to play only a minor role. Importantly, our calculations indicate that the dominantly coherent transport may lead to an electronic charge distribution that does not follow the periodicity of the QCL structure for subthreshold voltages.

## ACKNOWLEDGMENTS

This work has been supported by the Austrian Scientific Fund FWF (SFB-ADLIS, SFB-IRON, DK CoQuS), the Austrian nanoinitiative project PLATON, the Deutsche Forschungsgemeinschaft (Grants No. SFB 631 and No. SPP 1285), and the Excellence Cluster Nanosystems Initiative Munich. We acknowledge clarifying discussions with A. Wacker and C. Jirauschek.

*tillmann.kubis@wsi.tum.de

[1] C. Gmachl, F. Capasso, D. L. Sivco, and A. Y. Cho, Rep. Prog. Phys. **64**, 1533 (2001).

[2] R. Köhler, A. Tredicucci, F. Beltram, H. E. Beere, E. H. Linfield, A. G. Davies, D. A. Ritchie, R. C. Iotti, and F. Rossi, Nature (London) **417**, 156 (2002).

[3] A. W. M. Lee, Q. Qin, S. Kumar, B. S. Williams, Q. Hu, and J. L. Reno, Appl. Phys. Lett. **89**, 141125 (2006).

[4] C. Walther, M. Fischer, G. Scalari, R. Terazzi, N. Hoyler, and J. Faist, Appl. Phys. Lett. **91**, 131122 (2007).

[5] M. A. Belkin, F. Capasso, F. Xie, A. Belyanin, M. Fischer, A. Wittmann, and J. Faist, Appl. Phys. Lett. **92**, 201101 (2008).

[6] S. Kumar, Q. Hu, and J. L. Reno, Appl. Phys. Lett. **94**, 131105 (2009).

[7] R. C. Iotti and F. Rossi, Phys. Rev. Lett. **87**, 146603 (2001).
[8] C. Jirauschek, G. Scarpa, P. Lugli, M. Vitiello, and G. Scamarcio, J. Appl. Phys. **101**, 086109 (2007).
[9] S.-C. Lee and A. Wacker, Phys. Rev. B **66**, 245314 (2002).
[10] N. Vukmirović, Z. Ikonić, D. Indjin, and P. Harrison, Phys. Rev. B **76**, 245313 (2007).
[11] I. Savić, N. Vukmirović, Z. Ikonić, D. Indjin, R. W. Kelsall, P. Harrison, and V. Milanović, Phys. Rev. B **76**, 165310 (2007).
[12] S.-C. Lee and A. Wacker, Appl. Phys. Lett. **83**, 2506 (2003).
[13] N. Vukmirović, D. Indjin, Z. Ikonić, and P. Harrison, IEEE Photon. Technol. Lett. **20**, 129 (2008).
[14] X. Zheng, W. Chen, M. Stroscio, and L. F. Register, Phys. Rev. B **73**, 245304 (2006).
[15] S.-C. Lee, F. Banit, M. Woerner, and A. Wacker, Phys. Rev. B **73**, 245320 (2006).
[16] A. Pecchia and A. D. Carlo, Rep. Prog. Phys. **67**, 1497 (2004).
[17] A. M. Andrews, A. Benz, C. Deutsch, G. Fasching, K. Unterrainer, P. Klang, W. Schrenk, and G. Strasser, Mater. Sci. Eng., B **147**, 152 (2008).
[18] A. Wacker, Phys. Rev. B **66**, 085326 (2002).
[19] R. Lake, G. Klimeck, R. C. Bowen, and D. Jovanovic, J. Appl. Phys. **81**, 7845 (1997).
[20] T. Kubis and P. Vogl, J. Comput. Electron. **6**, 183 (2007).
[21] U. Ekenberg, Phys. Rev. B **40**, 7714 (1989).
[22] X. Gao, D. Botez, and I. Knezevic, J. Appl. Phys. **103**, 073101 (2008).
[23] *Semiconductors: Intrinsic Poperties of Group IV Elements and III-V, II-VI and I-VII Compounds*, Landolt-Börnstein, New Series, edited by O. Madelung (Springer, Berlin, 1987), Group III, Vol. 22, Pt. a.
[24] H. Callebaut, S. Kumar, B. S. Williams, Q. Hu, and J. L. Reno, Appl. Phys. Lett. **84**, 645 (2004).
[25] M. Manenti, F. Compagnone, A. D. Carlo, and P. Lugli, J. Comput. Electron. **2**, 433 (2003).
[26] C. Jirauschek and P. Lugli, Phys. Status Solidi C **5**, 221 (2008).
[27] L. Hedin, Phys. Rev. **139**, A796 (1965).
[28] U. von Barth and B. Holm, Phys. Rev. B **54**, 8411 (1996).
[29] B. Holm and U. von Barth, Phys. Rev. B **57**, 2108 (1998).
[30] K. S. Thygesen and A. Rubio, Phys. Rev. B **77**, 115333 (2008).
[31] S. Datta, *Electronic Transport in Mesoscopic Systems* (Cambridge University Press, Cambridge, England, 1995).
[32] D. Mamaluy, D. Vasileska, M. Sabathil, T. Zibold, and P. Vogl, Phys. Rev. B **71**, 245321 (2005).
[33] T. Kubis, C. Yeh, and P. Vogl, J. Comput. Electron. **7**, 432 (2008).
[34] A. E. Siegman, *Lasers* (University Science Books, Mill Valley, California, 1986).
[35] F. Banit, S.-C. Lee, A. Knorr, and A. Wacker, Appl. Phys. Lett. **86**, 041108 (2005).
[36] S. Kohen, B. S. Williams, and Q. Hu, J. Appl. Phys. **97**, 053106 (2005).
[37] In calculating this spatial average, we leave out the areas close to the device boundaries that are influenced by the nonlocal scattering within the transition areas.
[38] A. Trellakis, A. T. Galick, A. Pacelli, and U. Ravaioli, J. Appl. Phys. **81**, 7880 (1997).
[39] B. S. Williams, H. Callebaut, S. Kumar, Q. Hu, and J. L. Reno, Appl. Phys. Lett. **82**, 1015 (2003).
[40] L. Ajili, G. Scalari, M. Giovannini, N. Hoyler, and J. Faist, J. Appl. Phys. **100**, 043102 (2006).
[41] H. C. Liu, M. Wächter, D. Ban, Z. R. Wasilewski, M. Buchanan, G. C. Aers, J. C. Cao, S. L. Feng, B. S. Williams, and Q. Hu, Appl. Phys. Lett. **87**, 141102 (2005).
[42] A. Benz, G. Fasching, A. M. Andrews, M. Martl, K. Unterrainer, T. Roch, W. Schrenk, S. Golka, and G. Strasser, Appl. Phys. Lett. **90**, 101107 (2007).
[43] S. L. Lu, L. Schrottke, S. W. Teitsworth, R. Hey, and H. T. Grahn, Phys. Rev. B **73**, 033311 (2006).
[44] V. D. Jovanović, D. Indjin, N. Vukmirović, Z. Ikonić, P. Harrison, E. H. Linfield, H. Page, X. Marcadet, C. Sirtori, C. Worrall, H. E. Beere, and D. A. Ritchie, Appl. Phys. Lett. **86**, 211117 (2005).
[45] H. Callebaut, S. Kumar, B. S. Williams, Q. Hu, and J. L. Reno, Appl. Phys. Lett. **83**, 207 (2003).
[46] M. S. Vitiello, G. Scarmacio, V. Spagnolo, B. S. Williams, S. Kumar, and Q. Hu, Appl. Phys. Lett. **86**, 111115 (2005).
[47] B. R. Nag, Semicond. Sci. Technol. **19**, 162 (2004).
[48] T. Unuma, M. Yoshita, T. Noda, H. Sakaki, and H. Akiyama, J. Appl. Phys. **93**, 1586 (2003).
[49] K. Leosson, J. R. Jensen, W. Langbein, and J. M. Hvam, Phys. Rev. B **61**, 10322 (2000).
[50] T. Roch, A. M. Andrew, G. Fasching, A. Benz, W. Schrenk, and K. Unterrainer, Cent. Eur. J. Phys. **5**, 244 (2007).
[51] R. Nelander and A. Wacker, Appl. Phys. Lett. **92**, 081102 (2008).
[52] R. C. Iotti and F. Rossi, Appl. Phys. Lett. **78**, 2902 (2001).